Rotational synchronization of camphor ribbons in different geometries

Jyoti Sharma, Ishant Tiwari, Dibyendu Das, and P. Parmananda
Department of Physics, Indian Institute of Technology, Bombay, Powai, Mumbai, Maharashtra 400076, India

Véronique Pimienta
Laboratoire des IMRCP, Université de Toulouse, CNRS UMR 5623, Université Paul Sabatier, Toulouse Cedex 9, France

(Received 22 January 2020; revised manuscript received 1 April 2020; accepted 5 April 2020; published 4 May 2020)

We present experiments on multiple pinned self-propelled camphor ribbons, which is a rectangular piece of paper with camphor infused in its matrix. Experiments were performed on three, four, and five ribbons placed in linear and polygonal geometries. The pinned ribbons rotate on the surface of water, due to the surface tension gradient introduced by the camphor layer in the neighborhood of the ribbon. This camphor layer leads to a chemical coupling between the ribbons. In different geometries, the ribbons have been observed to rotationally synchronize in all the possible configurations. A numerical model, emulating the interactions between the ribbons as Yukawa interaction was studied, which was qualitatively able to reproduce the experimental findings.

DOI: 10.1103/PhysRevE.101.052202

I. INTRODUCTION

Collective behavior of two or more coupled oscillators is widely studied in different areas of science. This collective behavior can give rise to interesting phenomena like pattern formation [1–4], partially synchronized states [5], amplitude death [6–8], mutual entrainment [9], phase flip [10], chimera [11–13], clustering [13,14], swarming [15], etc. Besides these, one of the key occurrences is the emergence of synchronization [16], which is the rhythmical behavior of two or more coupled oscillators. Synchronization has been reported in a variety of chemical [17–21], physical [22,23], biological [24,25], and ecological [26,27] systems. Moreover, the fingerprint of synchronization has been found in large complex networks [28]. The geometry and coupling mechanism of the network plays an important role in determining the properties of the observed phenomena [29]. Coupling and geometry plays an important role not only in complex networks but also in mechanical systems like the synchronized activity of rotating pendula placed in different geometries [22].

In this paper, we have studied the rotational synchronization of self-propelled [30] camphor ribbons placed in different geometries. A camphor ribbon is a rectangular piece of paper with camphor infused in it. The ribbon, when placed on the surface of water, exhibits spontaneous motion. This motion is caused by the surface tension gradients introduced by the inhomogeneously distributed camphor layer around the ribbon [31,32]. Van der Mensbrugghe explained this motion in 1869 [31]. Since then, this system has been extensively studied both experimentally and theoretically [32–35].

A camphor particle placed on the surface of water shows translational, rotational, and intermittent motion [36]. Various shapes of such particles, such as the shape of a comma, or a crescent moon [32] or a disk [37] have been studied. Frenkel *et al.* [38] and Koyano *et al.* [39] have studied a single camphor rotor. A camphor engine has been realized as a mini generator of electricity recently [40]. The camphor layer of one camphor loaded particle interacts with the camphor layer of another, which leads to the chemical coupling between them [32,41]. This coupling leads to the synchronization of the camphor particles. The translational synchronization of camphor boats in circular, triangular, and square-shaped channels has been studied in Refs. [42,43]. However, rotational synchronization of two camphor ribbons has been reported only recently [41] in 2019, in which two modes of the synchronization in coupled camphor ribbons were observed. In one of the modes, both ribbons rotate in the same direction (corotating synchronization) while in the other mode both the ribbons rotate in opposite directions (counter-rotating synchronization). Furthermore, it was experimentally observed that the counter-rotating mode of the synchronization was more robust than the corotating one.

This paper deals with the collective dynamics of multiple camphor ribbons placed in different geometries. Experiments were performed on three, four, and five camphor ribbons. The geometries under study were open (linear), polygonal (triangle and square), and star. The different rotationally synchronized configurations observed are reported. Furthermore, the preference of the counter-rotating mode of synchrony over the corotating mode, in experiments involving three coupled rotators placed in a triangular geometry, was investigated.

A numerical model, considering ribbons as point particles moving on a circle and mimicking the interactions between them as a Yukawa-like potential [44] is also presented. The present model is slightly different from the numerical model for two camphor ribbons studied previously [41]. The model has qualitatively verified our experimental findings.

The manuscript is divided into four sections: Introduction (Sec. I), Experiments (Sec. II), Numerical Model (Sec. III), and Summary and Discussion (Sec. IV). Furthermore, Sec. II is divided into two subsections that describe the experimental protocol and results. Similarly, Sec. III is divided into two

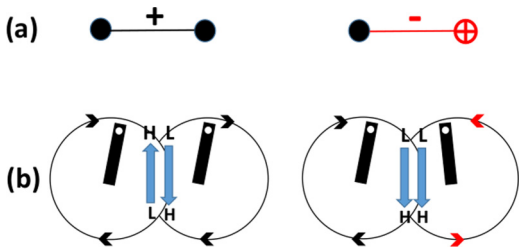

FIG. 1. Schematic diagram of two corotating and counter-rotating camphor ribbons. (a) Two black blobs show the same direction of the rotation of the ribbons, while one black and other red (crossed) blob represents the opposite direction of rotation of ribbons. The corotating (black line) and counter-rotating (red line) are represented with a + and − sign, respectively. In (b), L and H correspond to the low and high surface tension. The arrows show the direction of the rotation of the ribbons.

subsections describing the numerical model and the simulation results.

II. EXPERIMENTS

Experiments were performed on multiple camphor ribbons placed in different geometries. The number of ribbons studied was 3,4, and 5. The three-camphor-ribbons setup was studied on a linear and a triangular geometry, while the four ribbons were studied on linear and square geometry. For the case of five ribbons, only the star configuration has been studied. The ribbons were placed on the surface of water and their dynamics were recorded with a camera.

The two ribbons are said to be in corotating (counter-rotating) configuaration, if both of them rotate in the same (opposite) sense of rotation (see Fig. 1). If a pair of rotators is synchronized in the corotating (counter-rotating) configuration, then it will be considered to be sharing a corotating (counter-rotating) bond. A bond will be denoted by a plus (+) and a minus (−) sign for the corotating and counter-rotating cases respectively, as shown in Fig. 1(a). Experiments on two camphor ribbons had shown that the counter-rotating (−) mode of synchronization was preferred over the corotating (+) one [41]. It can be understood with the following intuitive argument: Since the ribbons move in the direction of higher surface tension, the direction of surface tension gradient is fixed in the common region between the pivots for the case of counter-rotating synchronization [Fig. 1(b)]. In contrast, for the corotating scenario, there must be a gradient reversal or switching at this common region [Fig. 1(b)] every time a ribbon passes through it. This state of the continuous gradient switching in a small spatial region, in our opinion, should be less favorable than to maintain a static gradient in the case of counter-rotating synchronized state.

In the present work, multiple ribbons placed in different geometries will have several synchronized configurations. To represent these configurations, we will adopt a convention identical to the one used to describe Fig. 1(a) in the preceding paragraph, albeit applied to multiple pairs of rotators that are present in each configuration. We will refer to a configuration in terms of the bonds (corotating vs. counter-rotating) that are present in it. Since we are only interested in the type of bond (co- vs. counter-rotating) between the pair of ribbons, the direction of the rotation of a single ribbon in that bond, is redundant in defining the configuration. The details of the configurations present in a given geometry will be discussed in the results section.

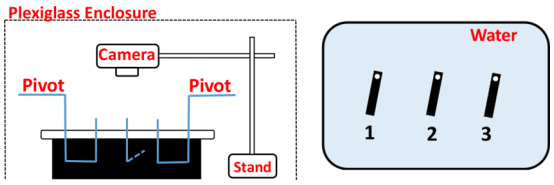

FIG. 2. Side view (left) and camera view (right) of the experimental setup for three camphor ribbons placed on the surface of water in a linear geometry. The general experimental setup, except for the number of rotators, is same for all the other geometries and the number of the camphor ribbons.

A. Protocol

The experiments were performed in a glass container of dimensions 25 cm × 25 cm × 4 cm. The container is placed inside a plexiglass enclosure to prevent air drafts from interfering with the dynamics of the system. Figure 2 shows the schematic diagram of the side and camera view of the experimental setup for three ribbons placed on a line. The general setup, except for the number of rotators, is the same for all the other experiments. The glass container is filled with 800 ml of water (MilliQ). The room temperature for all the experiments is set between 24.2°C and 24.8°C. A high-speed video camera (GoPro Hero-4, frame rate 120 Hz, 720p resolution) is installed inside the glass box to record the rotators dynamics.

The desired number of camphor ribbons were prepared by cutting rectangular ribbons of dimensions 2.2 cm × 0.5 cm from a clean A4 size paper sheet. The ribbons were kept black in color with a white circular region at one end to aid with the motion tracking of the rotators. A hole was made with a needle at the other end of each paper ribbon. A 1.21 M solution of laboratory grade camphor in ethanol was poured onto each ribbon. The ribbons were left in the poured solution for 60 s and were then subsequently left to dry in the air for 600 s. Finally, the ribbons were pivoted on a thin wire (blue wire in the left panel of Fig. 2) and were placed on the surface of the water to observe their rotational motion.

The pivots were brought together in the geometry under study before putting the ribbons on the surface of the water. The pivot-to-pivot distance between the nearest-neighboring ribbons was kept constant at 3 cm in each geometry. The first 360 s of data was removed as transients, and then the data were recorded for the next 180 s. The recorded data for each configuration were analyzed with a particle tracking code in the MATLAB environment, written by Daniel Blair and Eric Dufresne [45]. This code is based on the particle tracking algorithms of Crocker and Grier [46]. The white dots on the ribbons (see supplemental videos [47]) were tracked using the above-mentioned codes. The positions of the tracked dots are (x_i, y_i), $i = 1, 2,..., N$ where N is the total number of ribbons in the experiment. For brevity, we will refer to the

positions of these white dots as the positions of the ribbons itself throughout the manuscript.

It should be noted that the initial direction of rotation of the ribbons, i.e., clockwise or anticlockwise, is decided by the initial fluctuations in the system. Hence, the initial configuration in which the system will land is decided randomly. However, one can perturb the system externally to get to a desired configuration.

B. Results

To reiterate, the experiments were performed on three, four, and five ribbons on different geometries. The ribbons are found to synchronize in the geometries studied. The various configurations found in experiments are presented in the section.

1. Three ribbons

In this subsection, we will discuss the results of three rotators in linear and triangular geometries respectively, and the corresponding results are presented in Figs. 3 and 4. The dynamics of the one representative configuration is shown for both the geometries.

(a) In a line. The three ribbons placed in a line will have two bonds [one bond for each pair (1,2) and (2,3) in Fig. 2], and hence three configurations are possible as per our bond convention. These configurations [Fig. 3(a)] are as follows: configuration (1), where both bonds are corotating, i.e., $+\ +$; configuration (2), where one bond is corotating while the other is counter-rotating, i.e., $+\ -$; and configuration (3), where both bonds are counter-rotating, i.e., $-\ -$. Furthermore, we can achieve other one corotating and one counter-rotating configuration, i.e., $-\ +$, on changing the position of the bonds of $+\ -$ configuration. However, as we are defining the configurations with respect to the type of the bonds present in it and not their positions, we will club both these sister configurations ($+\ -$ and $-\ +$) as one ($+\ -$). In Fig. 3(b), the temporal evolution of (x_1, x_2, x_3) and (y_1, y_2, y_3) positions of the rotators are plotted for a duration of 10 s. The corresponding phase plots for $[(x_1, x_2), (x_2, x_3), (x_1, x_3)]$ and $[(y_1, y_2), (y_2, y_3), (y_1, y_3)]$ are plotted in Fig. 3(c) from data recorded for 180 s.

In the experiments, the ribbons have synchronized in all three configurations. However, for the sake of conciseness, we present the dynamics [Figs. 3(b) and 3(c)] for configuration $-\ -$, and the corresponding video (1.mp4) is provided in the Supplemental Material [47]. The time evolution of the (x_1, x_2, x_3) and (y_1, y_2, y_3) positions [Fig. 3(b)] of the three ribbons shows that the ribbons are synchronized. The phase plots [Fig. 3(c)] clearly show that the x positions of all the ribbon pairs are in-phase lag synchronized. However, the y positions of the first and second ribbon pair (y_1, y_2) and the second and the third ribbon pair (y_2, y_3) are out-of-phase lag synchronized. This type of the synchronization is defined as mirror synchronization [22].

(b) On a triangle. In contrast to the linear case, three ribbons placed in a polygonal, i.e., triangular, geometry can have three bonds. One can think of $+\ +\ +$, $+\ +\ -$, $+\ -\ -$, and $-\ -\ -$ as possible configurations, but the triangular geometry rules out the possibility of the $+\ +\ -$ and $-\ -\ -$

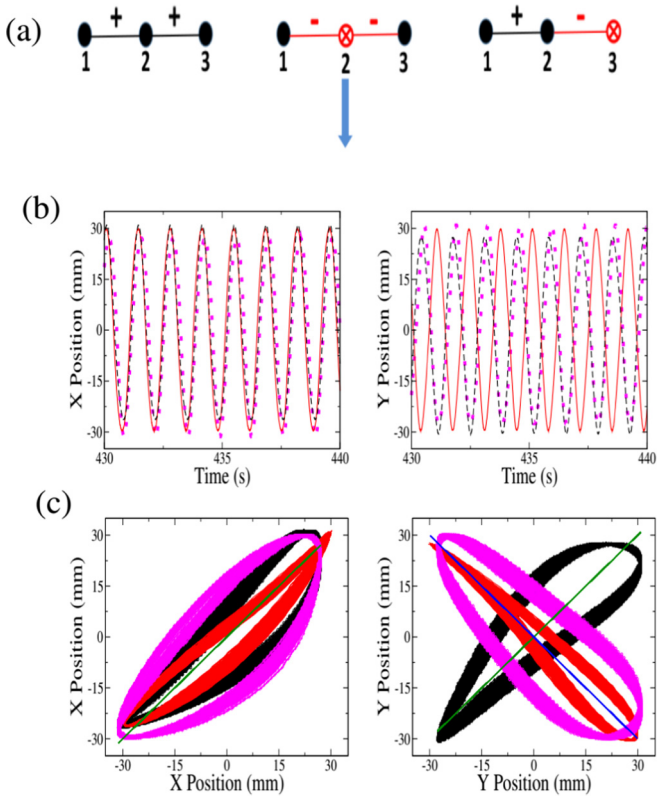

FIG. 3. For three camphor ribbons placed on a line, (a) shows the schematic of the three possible configurations, i.e., $+\ +$, $-\ -$, and $+\ -$. The dynamics is shown for configuration $-\ -$. The magenta (dotted), red (solid), and black (dashed) lines in (b) correspond to the temporal evolution of the (x_1, x_2, x_3) position (left) and (y_1, y_2, y_3) position (right) of the first (1), second (2), and third (3) camphor ribbons, respectively. (c) The phase plots of x (left) and y (right) positions of the camphor ribbons. Magenta (solid), red (circle), and black (plus) represent phase plot of (x_1, x_2), (x_2, x_3), (x_1, x_3) (left) and (y_1, y_2), (y_2, y_3), (y_1, y_3) (right), respectively. The solid green and blue lines are of slopes 1 and -1, respectively. (x_1, x_2), (x_2, x_3), (x_1, x_3), and (y_1, y_3) are in-phase lag synchronized (along line of slope 1) while (y_1, y_2) and (y_2, y_3) are out-of-phase lag synchronized (along the line of slope -1).

configurations because of the constraint of a closed geometry. A closed triangular geometry allows for only two bonds to be chosen independently, while the third one is dictated by the choice of the two independent bonds. Hence, only two configurations, namely all rotator pairs corotating synchronized ($+\ +\ +$) and one corotating and two counter-rotating synchronized ($+\ -\ -$), are possible and are also observed experimentally [Fig. 4(a)]. Furthermore, as explained above, $+\ -\ -$ will have two more sister configurations by changing the positions of the bonds. These three sister configurations are grouped together as the configuration $+\ -\ -$. In experiments, all the configurations were found to rotationally synchronize. However, the direct evidence of the synchronized motion of rotators (Figs. 4(b) and 4(c)] is shown only for configuration $+\ +\ +$. The corresponding video (2.mp4) is provided in the Supplemental Material [47]. In Fig. 4(b), the temporal evolution of (x_1, x_2, x_3) and (y_1, y_2, y_3) position of each rotator is plotted for a duration of 10 s. The corresponding phase plots

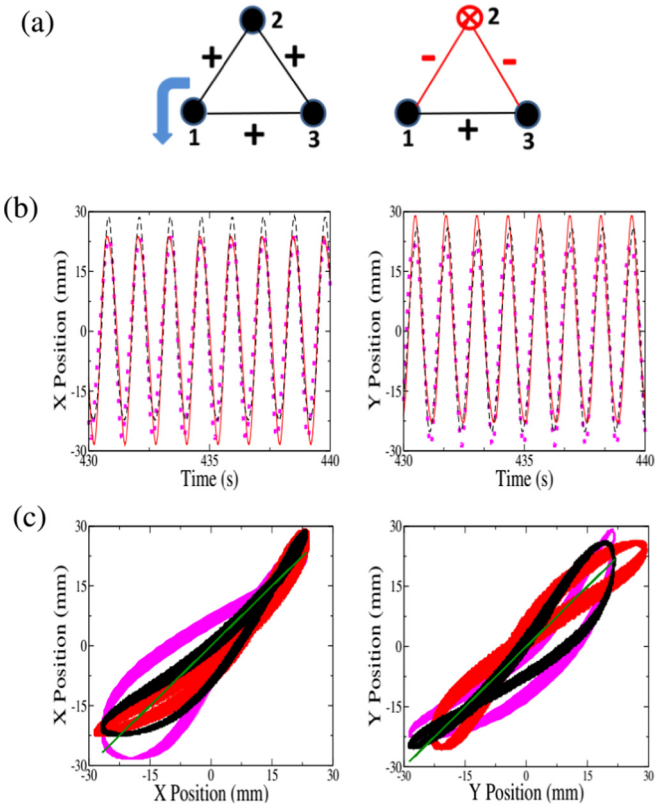

FIG. 4. For three camphor ribbons placed on a triangle panel (a) shows the schematic for the configurations $+++$ and $+--$. The plots in (b) and (c) correspond to the $+++$ configuration. The magenta (dotted), red (solid) and black (dotted) lines in (b) correspond to the temporal evolution of (x_1, x_2, x_3) position (left) and (y_1, y_2, y_3) position (right) of the first (1), second (2), and third (3) camphor ribbons, respectively. (c) The phase plots of x (left) and y (right) positions of the camphor ribbons. Magenta (solid), red (circle), and black (plus) represent phase plots of (x_1, x_2), (x_2, x_3), (x_1, x_3) (left side) and (y_1, y_2), (y_2, y_3), (y_1, y_3) (right side), respectively. The solid green is a line of slope 1. All the x and y positions of the ribbons are in-phase synchronized (along the line of slope 1).

for $[(x_1, x_2), (x_2, x_3), (x_1, x_3)]$ and $[(y_1, y_2), (y_2, y_3), (y_1, y_3)]$ are plotted in Fig. 4(c) from data recorded for 180 s. It is evident that all three pairs of rotators are in-phase lag synchronized (configuration $+++$).

As explained earlier [Fig. 1(b)], two coupled camphor ribbons have an affinity toward being counter-rotating synchronized than being corotating synchronized [41]. This motivated us to study the presence of any preference toward a specific synchronized configuration for multiple ribbons in a given geometry. However, we chose to study only the triangular geometry for this purpose. The choice of triangular geometry over all the other geometries studied in the present work can be justified with two reasons: First, it is a geometrically frustrated configuration and, second, it has minimum number of configurations (two) which reduces the requirement for collection of a large dataset to observe a preferential trend toward a specific synchronized configuration.

Twenty-five experiments starting from the same initial conditions were performed on three ribbons placed in a triangular geometry. In all the experiments, after some transient dynamics, ribbons synchronized in either $+++$ or $+--$ configurations. Of these 25 experiments, the $+--$ configuration (or its sister configurations, i.e., $-+-$ and $--+$) was observed 21 times while the $+++$ configuration was observed only four times. This observation indicates that three ribbons placed on a triangle prefer to be in the configuration having more number of counter-rotating $(-)$ bonds over the one having all corotating $(+)$ bonds. This finding is in line with the experimental observation for two ribbons [41]. Furthermore, the $+--$, $-+-$, and $--+$ configurations are reminiscent of classical spins placed on a frustrated triangular geometry with antiferromagnetic interactions between them [48].

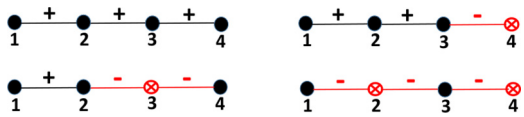

FIG. 5. The schematic diagram of the configurations observed in the experiments for four camphor ribbons placed in a linear geometry. The configurations are $+++$, $++-$, $+--$, and $---$.

2. *Four ribbons*

In this subsection, we study the various synchronization states observed when four camphor ribbons are coupled together in different geometries. The setup and protocol for these experiments are mentioned in Sec. IIA, the only change being the number of rotators.

(a) On a line. Four ribbons placed in a line will have three bonds and a total of four configurations. As mentioned previously in the experimental section, they are $+++$, $++-$, $+--$, and $---$ as shown in Fig. 5. There are three sister configurations represented by $++-$ ($++-$, $+-+$, $-++$) and $+--$ ($+--$, $-+-$, $--+$) by changing the positions of the bonds. All the configurations mentioned above were observed experimentally. The detailed proof of the synchronization and the corresponding video (3.mp4) is shown for the configuration $+--$ in the Supplemental Material [47] (Fig. 2, Supplemental Material [49]).

(b) On a square. On placing four camphor ribbons on a closed (square) geometry the number of bonds increase to 4. But the closed nature of this geometry constrains the independent choice of bonds to only three, the fourth one being dependent on the other three bonds. This constraint rules out the existence of configurations $+++-$ and $+---$. Therefore, only the $++++$, $++--$, and $----$ configurations are possible and observed experimentally. It is again to be noted that the configuration $++--$ represents six sister configurations ($++--$, $-++-$, $--++$, $+-+-$, $-+-+$, $+--+$). These sister configurations have the same type of bonds but differ by their individual positions. The experiments yielded all the above-mentioned synchronized configurations (Fig. 6). For the configuration $++--$, the phase plots and the corresponding video (4.mp4) is provided in the Supplemental Material [47] (Fig. 3, Supplemental Material [49]).

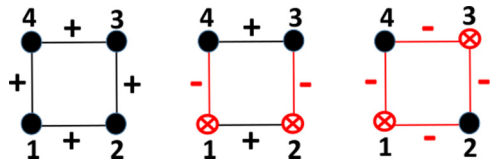

FIG. 6. The schematic diagram of the configurations observed in the experiments for four camphor ribbons placed in a square geometry. The configurations are $+\ +\ +\ +$, $+\ +\ -\ -$, and $-\ -\ -\ -$.

3. Five ribbons

Finally, experiments performed by keeping five camphor ribbons in a star-shaped geometry (Fig. 7) are presented in this subsection. The setup and protocol for these experiments is mentioned in Sec. IIA previously.

The degree of a node in network theory is defined as the number of nodes to which it is connected. Similarly, in our experiments, we can define the degree of a rotator as the number of rotators to which it is strongly coupled, i.e., which are present at a pivot to pivot distance 3 cm from it. A star network topology (Fig. 7) for five rotators is interesting as the degree of the central rotator (degree = 4) is four times that of the peripheral rotators (degree = 1). This disparity in degrees of the rotators is significantly larger when compared to the previously studied topologies (line, triangle, square). Besides, one can intuit that the environment of the central oscillator would have a higher concentration of camphor since rotators surround it on all four sides. These contrasting differences between the previously presented geometries and the star geometry merit its inclusion in this work. In this geometry, ribbons can have five main configurations (Fig. 7), namely $+\ +\ +\ +$, $+\ +\ +\ -$ (four sister configurations: $+\ +\ +\ -$, $+\ +\ -\ +$, $+\ -\ +\ +$, $-\ +\ +\ +$), $+\ +\ -\ -$ (six sister configurations: $+\ +\ -\ -$, $-\ +\ +\ -$, $-\ -\ +\ +$, $+\ -\ +\ -$, $-\ +\ -\ +$, $+\ -\ -\ +$), $+\ -\ -\ -$ (four sister configurations: $+\ -\ -\ -$, $-\ +\ -\ -$, $-\ -\ +\ -$, $-\ -\ -\ +$), and $-\ -\ -\ -$. In the experiments, the ribbons successfully synchronized in all the configurations mentioned above. Therefore, we can infer that a disparity in the degree of the rotators being coupled (central vs. peripheral) does not have a significant effect on their possible modes of synchrony. The detailed dynamics are presented for the configuration $+\ +\ +\ -$ along with the corresponding video (5.mp4) in the Supplemental Material [47] (Fig. 4, Supplemental Material [49]).

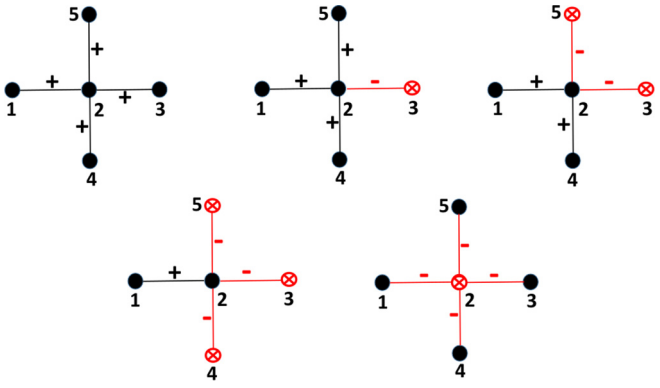

FIG. 7. The schematic diagram of the configurations observed in the experiments for five camphor ribbons placed in a star geometry. The configurations are $+\ +\ +\ +$, $+\ +\ +\ -$, $+\ +\ -\ -$, $+\ -\ -\ -$, and $-\ -\ -\ -$.

III. NUMERICAL MODEL

To model the system, we have considered the camphor ribbons as point particles of unit mass. The point particles are placed on a unit circle. The center of their respective circles can be considered as the pivot in the experiments. The position of the pivot (center) depends on the geometry in which the ribbons are placed. The following text gives the numerical model and the results for the three interacting particles (linear and triangular geometry). The equations used for the other geometries can be found in the Appendix.

A. Linear geometry

Let (r_i, θ_i) denote the position of the ith ($i = 1, \ldots, N$, where N is the total number of particles) particle placed on a linear geometry with respect to the origin (0,0). The position of the center of the circle of the first and ith particle is (0,0) and $(il,0)$, respectively, for a fixed distance l between nearest-neighboring pivots. The experimentally observed repulsive coupling [14] between the ribbons, is mimicked through a repulsive Yukawa potential in the model. At any time t, for a distance $r(t)$ between the point particles, the Yukawa potential is $V[r(t)] = \frac{e^{-Kr(t)}}{r(t)}$, where K is inversely related to the range and the force due to this potential is $\frac{e^{-Kr(t)}}{r(t)^2}[1 + Kr(t)]$. The radial component of the Yukawa force is assumed to be balanced by the pivot constraint force. Therefore, only the tangential component of the force acts on the particles and determines their dynamics. For the ith point particle placed on a line, tangential component of the force can be written as:

$$F_T(t)_i = \sum_{j=1, j\neq i}^{N} \frac{e^{-Kr_{ij}(t)}}{r_{ij}^3(t)}[1 + Kr_{ij}(t)][\sin(\theta_i - \theta_j) + (j-i)l\sin(\theta_i)], \quad (1)$$

where N is the total number of particles. The equations governing the dynamics of the ith point particle having natural frequency Ω_i are as follows:

$$\dot{\theta}_i(t) = \omega_i(t) \quad i = 1, 2, \ldots, N, \quad (2)$$

$$\dot{\omega}_i(t) = F_T(t)_i r_i(t) - C(\omega_i(t) - \Omega_i) \quad i = 1, 2, \ldots, N, \quad (3)$$

where the second term in Eq. (3) for $\dot{\omega}_i$ quantifies the tendency of the rotator to go to its autonomous frequency Ω_i if there are no other rotators.

B. Polygonal geometry

(a) On a triangle. Three point particles were placed in a triangular geometry with the centers of their respective circles, i.e., pivots at (0,0), $(\frac{l}{2}, \frac{\sqrt{3}}{2}l)$, and $(l, 0)$, for the first, second,

and third point particles. The tangential Yukawa force acting on the particles in this geometry is given as follows:

$$F_1 = \frac{e^{-kr_{12}}}{r_{12}^3}(1+kr_{12})\left[\sin(\theta_1-\theta_2)+l\sin\left(\theta_1-\frac{\pi}{3}\right)\right] + \frac{e^{-kr_{13}}}{r_{13}^3}(1+kr_{13})[\sin(\theta_1-\theta_3)+l\sin\theta_1], \quad (4)$$

$$F_2 = \frac{e^{-kr_{21}}}{r_{21}^3}(1+kr_{21})\left[\sin(\theta_2-\theta_1)-l\sin\left(\theta_2-\frac{\pi}{3}\right)\right] + \frac{e^{-kr_{23}}}{r_{23}^3}(1+kr_{23})\left[\sin(\theta_2-\theta_3)+l\sin\left(\theta_2+\frac{\pi}{3}\right)\right], \quad (5)$$

$$F_3 = \frac{e^{-kr_{31}}}{r_{31}^3}(1+kr_{31})[\sin(\theta_3-\theta_1)-l\sin\theta_3] + \frac{e^{-kr_{32}}}{r_{32}^3}(1+kr_{23})\left[\sin(\theta_3-\theta_2)-l\sin\left(\theta_3+\frac{\pi}{3}\right)\right]. \quad (6)$$

The corresponding equations for four interacting particles placed in a square geometry and five interacting particles in a star geometry are provided in the Appendix.

C. Numerical results

The equations as mentioned above were simulated using a Runga-Kutta fourth-order method with a time step 10^{-4}. The first 1000 time units were discarded as transients, and the evolution in the next 1000 time units was analyzed. The value of r_i for $i = 1, \ldots, N$ was set to be one unit. Considering the fact that in the real experiments the force between the ribbons does not diverge at small separations, we have put a maximum bound $[(F_{\text{total}})_{\max}]$ on the magnitude of the total force experienced by each particle [right-hand side of Eq. (3)]. To account for the fact that in the experiments, all the ribbons are not perfectly identical, a slight random mismatch is introduced in the autonomous angular frequencies (Ω_i) of the point particles. The value of the initial phase θ_i was chosen randomly. The initial value of ω_i was kept equal to their respective autonomous angular frequency Ω_i. The sign of the Ω_i was chosen depending on the configuration in which point particles were placed. However, the parameters l, K, C, and $[(F_{\text{total}})_{\max}]$ were kept constant at a value 1.5, 1.5, 0.5, and 0.3 units, respectively, throughout the simulations, for all the geometries and their configurations. In a given geometry, all the experimentally observed configurations have been reproduced in the simulations. For the sake of consistency in this paper, the proof of synchronization is presented for only three particles (linear and triangular geometry). However, the detailed dynamics of the four and the five particles is presented in the Supplemental Material [49].

1. On a line

For three interacting particles on a line, the number of possible configurations and their nomenclature is identical to their experimental counterparts in Sec. IIB1. Experimental results shown in Fig. 3 are qualitatively reproduced in Fig. 8,

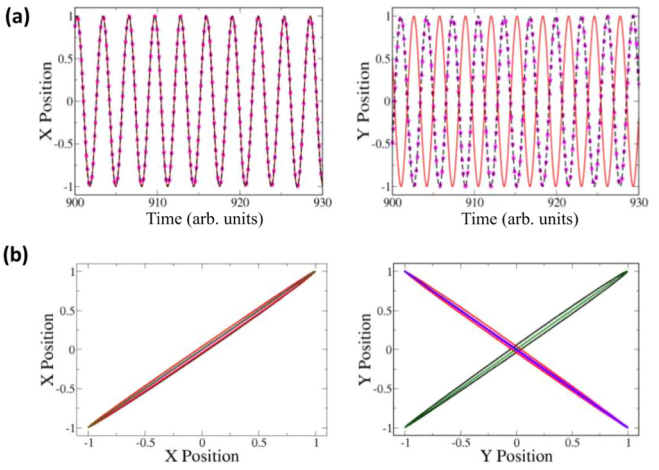

FIG. 8. For the linear geometry, the x position $x_i = \cos(\theta_i)$ and y position $y_i = \sin(\theta_i)$ for the ith point particle. The magenta (dotted), red (solid), and black (dashed) lines in (a) correspond to the temporal evolution of the x position (left) and y position (right) of the first, second, and third point particles, respectively. (b) The phase plots of x (left) and y (right) positions of the point particles for linear geometry. Here the magenta, red, and black curves represent phase plots of (x_1, x_2), (x_2, x_3), (x_1, x_3) (left side) and (y_1, y_2), (y_2, y_3), and (y_1, y_3) (right side), respectively. The solid green and blue lines are a line of slope 1 and -1, respectively. (x_1, x_2), (x_2, x_3), (x_1, x_3), and (y_1, y_3) are in-phase lag synchronized (along line of slope 1) while (y_1, y_2) and (y_2, y_3) are out-of-phase lag synchronized (along the line of slope -1).

which shows the simulation results of the configuration $- -$ for three interacting particles placed linearly. We can achieve other configurations in the simulations by changing the sign of the autonomous frequencies Ω_i (where $i = 1, 2, 3$). For example, all positive Ω_i will correspond to the configuration $+ + +$ in Fig. 3(a). The temporal behavior of the x position $[x_i = \cos(\theta_i)]$ and the y position $[y_i = \sin(\theta_i)]$ are plotted in Fig. 8(a). The x positions of all the particles (x_1, x_2, x_3) and the y positions of particles one and three (y_1, y_3) are synchronized in-phase. However, the y positions of the nearest-neighbor particles (y_1 and y_2; y_2 and y_3) are out-of-phase synchronized.

2. On a triangle

In the case of three interacting point particles placed on a triangle, the possible synchronized configurations simulated are identical to the experimentally observed configurations in the same geometry. The simulation results are presented for the configuration $+ + +$ in Fig. 9. The x $[x_i = \cos(\theta_i)]$ position (left panel) and y $[y_i = \sin(\theta_i)]$ position (right panel) of all the particles are in phase synchronized. The other configuration of this geometry, i.e., $+ - +$ can be achieved by changing the sign of Ω_2 placed at pivot position $(\frac{l}{2}, \frac{\sqrt{3}}{2}l)$.

IV. SUMMARY AND DISCUSSION

In this work, experiments on multiple coupled camphor ribbons were presented. The camphor ribbon, when placed on the surface of water, forms a camphor layer around it. This camphor layer leads to a decrease in the surface tension

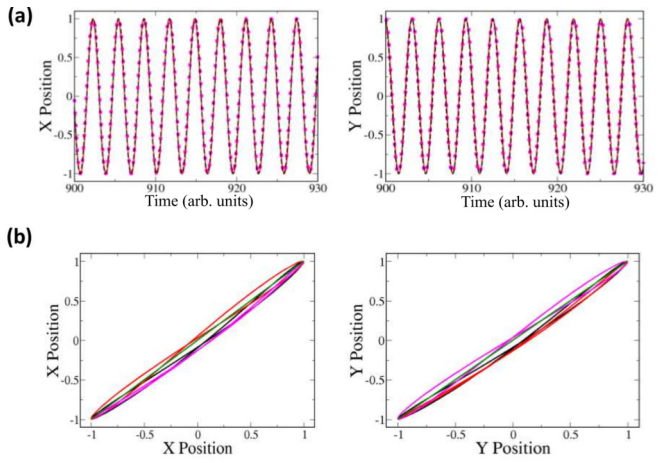

FIG. 9. For the triangular geometry, the x position $x_i = \cos(\theta_i)$ and y position $y_i = \sin(\theta_i)$ for the ith point particle. The magenta (dotted), red (solid), and black (dotted) lines in (a) correspond to the temporal evolution of the x position (left) and y position (right) of the first, second, and third point particles, respectively. (b) Shows the phase plots of x (left) and y (right) positions of the point particles for the triangle. The magenta, red, and black curves represent phase plots of (x_1, x_2), (x_2, x_3), (x_1, x_3) (left side) and (y_1, y_2), (y_2, y_3), (y_1, y_3) (right side), respectively. All the x and y positions of the ribbons are in-phase synchronized.

around the ribbon. The initial fluctuations in the distribution of this camphor layer create spatial inhomogeneities in it, which further lead to a net force acting on the ribbons. The camphor layer around one ribbon interacts with the camphor layer around the other ribbon, which leads to the chemical coupling between them. Furthermore, the coupling between the ribbons is repulsive in nature.

This coupling leads to synchronized rotational motion of the camphor ribbons. The strength of the coupling between the ribbons is distance dependent. Hence, the ribbons are rotationally synchronized only when the pivot to pivot distance between the adjacent ribbons is less than twice the length of a single ribbon. Lag synchronization was observed in linear and polygonal geometries for multiple (three, four, and five) coupled camphor rotators. All the configurations which are possible in a given geometry were observed experimentally. In the linear geometry, for a fixed number of ribbons, the number of the configurations observed is more than that of the polygonal geometry.

Experiments on three ribbons kept on a triangular geometry have shown that the configuration having the maximum number of counter-rotating bonds $(+\ -\ -)$ is preferred over the one having all corotating bonds $(+\ +\ +)$. The $+\ -\ -$ configuration represents three sister configurations where the positions of the individual bonds change. These three sister configurations were found to be equally probable among themselves. This is reminiscent of the degeneracy of multiple configurations of classical spins placed on a triangular lattice and having antiferromagnetic interactions between them [48].

A simulation model considering the ribbons as point particles has been formulated. This model accounts for the repulsive coupling between the ribbons using a repulsive Yukawa potential. This elementary choice of the Yukawa potential gives the freedom to tune the distance-dependent coupling observed in the experiments, with the parameter K of the Yukawa potential. The point particle simulations were able to reproduce the experimental findings qualitatively in different geometries.

We believe that these tabletop experiments on self-propelled rotators can find potential applications in the fields of active matter. A self-propelled camphor rotator can be compared with a classical spin. In the future, one can properly study this analogy and can find the probability of occurrence of the different configurations of camphor rotators and compare them with the spin systems kept in similar geometries.

ACKNOWLEDGMENTS

We acknowledge financial support from DST (India) (Grant No. EMR/2016/000275). J.S. thanks MHRD and IITB for financial support. I.T. acknowledges financial support from CSIR, India. Fruitful discussions with the Non-Linear Dynamics laboratory and the Statistical Mechanics laboratory at IITB are also acknowledged.

APPENDIX

1. On a square

Four point particles were placed in a square geometry with the centers of their respective circles, i.e., pivots at (0,0), (l,0), (l, l), and (0,l) for the first, second, third, and fourth point particles. The tangential Yukawa force acting on the particles in this geometry is given as follows:

$$F_1 = \frac{e^{-kr_{12}}}{r_{12}^3}(1+kr_{12})[\sin(\theta_1-\theta_2)+l\sin\theta_1] + \frac{e^{-kr_{13}}}{r_{13}^3}(1+kr_{13})[\sin(\theta_1-\theta_3)+l(\sin\theta_1-\cos\theta_1)] + \frac{e^{-kr_{14}}}{r_{14}^3}(1+kr_{14})[\sin(\theta_1-\theta_4)-l\cos\theta_1], \tag{A1}$$

$$F_2 = \frac{e^{-kr_{21}}}{r_{21}^3}(1+kr_{21})[\sin(\theta_2-\theta_1)-l\sin\theta_2] + \frac{e^{-kr_{23}}}{r_{23}^3}(1+kr_{23})[\sin(\theta_2-\theta_3)-l\cos\theta_2] + \frac{e^{-kr_{24}}}{r_{24}^3}(1+kr_{24})[\sin(\theta_2-\theta_4)-l(\sin\theta_2+\cos\theta_2], \tag{A2}$$

$$F_3 = \frac{e^{-kr_{31}}}{r_{31}^3}(1+kr_{31})[\sin(\theta_3-\theta_1)+l(\cos\theta_3-\sin\theta_3)] + \frac{e^{-kr_{32}}}{r_{32}^3}(1+kr_{32})[\sin(\theta_3-\theta_2)+l\cos\theta_3] + \frac{e^{-kr_{34}}}{r_{34}^3}(1+kr_{34})[\sin(\theta_3-\theta_4)-l\sin\theta_3], \tag{A3}$$

$$F_4 = \frac{e^{-kr_{41}}}{r_{41}^3}(1+kr_{41})[\sin(\theta_4-\theta_1)+l\cos\theta_4] + \frac{e^{-kr_{42}}}{r_{42}^3}(1+kr_{42})[\sin(\theta_4-\theta_2)+l(\sin\theta_4+\cos\theta_4)] + \frac{e^{-kr_{43}}}{r_{43}^3}(1+kr_{43})[\sin(\theta_4-\theta_3)+l\sin\theta_4]. \tag{A4}$$

2. On a star

Five point particles were placed in a star geometry with the centers of their respective circles, i.e., pivots, at (0,0), (l,0), ($2l$, 0), (l, l), and (l, $-l$) for the first, second, third, fourth, and fifth point particles. The tangential Yukawa force acting on the particles in this geometry is given as follows:

$$F_1 = \frac{e^{-kr_{12}}}{r_{12}^3}(1+kr_{12})[\sin(\theta_1-\theta_2)+l\sin\theta_1] + \frac{e^{-kr_{13}}}{r_{13}^3}(1+kr_{13})[\sin(\theta_1-\theta_3)+2l\sin\theta_1] + \frac{e^{-kr_{14}}}{r_{14}^3}(1+kr_{14})[\sin(\theta_1-\theta_4)+l(\sin\theta_1+\cos\theta_1)] + \frac{e^{-kr_{15}}}{r_{15}^3}(1+kr_{15})[\sin(\theta_1-\theta_5)+l(\sin\theta_1-\cos\theta_1)], \tag{A5}$$

$$F_2 = \frac{e^{-kr_{21}}}{r_{21}^3}(1+kr_{21})[\sin(\theta_2-\theta_1)-l\sin\theta_2] + \frac{e^{-kr_{23}}}{r_{23}^3}(1+kr_{23})[\sin(\theta_2-\theta_3)+l\sin\theta_2] + \frac{e^{-kr_{24}}}{r_{24}^3}(1+kr_{24})[\sin(\theta_2-\theta_4)+l\cos\theta_2] + \frac{e^{-kr_{25}}}{r_{25}^3}(1+kr_{25})[\sin(\theta_2-\theta_5)-l\cos\theta_2], \tag{A6}$$

$$F_3 = \frac{e^{-kr_{31}}}{r_{31}^3}(1+kr_{31})[\sin(\theta_3-\theta_1)-2l\sin\theta_3] + \frac{e^{-kr_{32}}}{r_{32}^3}(1+kr_{32})[\sin(\theta_3-\theta_2)-l\sin\theta_3] + \frac{e^{-kr_{34}}}{r_{34}^3}(1+kr_{34})[\sin(\theta_3-\theta_4)-l(\sin\theta_3-\cos\theta_3)] + \frac{e^{-kr_{35}}}{r_{35}^3}(1+kr_{35})[\sin(\theta_3-\theta_5)-l(\sin\theta_3+\cos\theta_3)], \tag{A7}$$

$$F_4 = \frac{e^{-kr_{41}}}{r_{41}^3}(1+kr_{41})[\sin(\theta_4-\theta_1)-l(\sin\theta_4+\cos\theta_4)] + \frac{e^{-kr_{42}}}{r_{42}^3}(1+kr_{42})[\sin(\theta_4-\theta_2)-l\cos\theta_4] + \frac{e^{-kr_{43}}}{r_{43}^3}(1+kr_{43})[\sin(\theta_4-\theta_3)+l(\sin\theta_4-\cos\theta_4)] + \frac{e^{-kr_{45}}}{r_{45}^3}(1+kr_{45})[\sin(\theta_4-\theta_5)-2l\cos\theta_4], \tag{A8}$$

$$F_5 = \frac{e^{-kr_{51}}}{r_{51}^3}(1+kr_{51})[\sin(\theta_5-\theta_1)-l(\sin\theta_5-\cos\theta_5)] + \frac{e^{-kr_{52}}}{r_{52}^3}(1+kr_{52})[\sin(\theta_5-\theta_2)+l\cos\theta_5] + \frac{e^{-kr_{53}}}{r_{53}^3}(1+kr_{53})[\sin(\theta_5-\theta_3)+l(\sin\theta_5+\cos\theta_5)] + \frac{e^{-kr_{54}}}{r_{54}^3}(1+kr_{54})[\sin(\theta_5-\theta_4)+2l\cos\theta_5]. \tag{A9}$$

[1] F. G. Kazanci and B. Ermentrout, SIAM J. Appl. Math. **67**, 512 (2007).

[2] N. E. Kouvaris, M. Sebek, A. S. Mikhailov, and I. Z. Kiss, Angew. Chem. **128**, 13461 (2016).

[3] S. Ducci, N. Treps, A. Maître, and C. Fabre, Phys. Rev. A **64**, 023803 (2001).

[4] X. Zhang, M. Fu, J. Xiao, and G. Hu, Phys. Rev. E **74**, 015202(R) (2006).

[5] P. Kumar, D. K. Verma, and P. Parmananda, Phys. Lett. A **381**, 2337 (2017).

[6] M. Dasgupta, M. Rivera, and P. Parmananda, Chaos **20**, 023126 (2010).

[7] T. Mandal, T. Singla, M. Rivera, and P. Parmananda, Chaos **23**, 013130 (2013).

[8] R. Phogat, I. Tiwari, P. Kumar, M. Rivera, and P. Parmananda, Eur. Phys. J. B **91**, 111 (2018).

[9] F. Montoya, M. Rivera, J. Escalona, and P. Parmananda, Phys. Lett. A **377**, 3124 (2013).

[10] J. M. Cruz, J. Escalona, P. Parmananda, R. Karnatak, A. Prasad, and R. Ramaswamy, Phys. Rev. E **81**, 046213 (2010).

[11] D. M. Abrams and S. H. Strogatz, Phys. Rev. Lett. **93**, 174102 (2004).

[12] C. Meena, K. Murali, and S. Sinha, Int. J. Bifurcat. Chaos **26**, 1630023 (2016).

[13] J. D. Hart, K. Bansal, T. E. Murphy, and R. Roy, Chaos **26**, 094801 (2016).
[14] H. Nishimori, N. J. Suematsu, and S. Nakata, J. Phys. Soc. Jpn. **86**, 101012 (2017).
[15] R. van Drongelen, A. Pal, C. P. Goodrich, and T. Idema, Phys. Rev. E **91**, 032706 (2015).
[16] A. Pikovsky, M. Rosenblum, and J. Kurths, *Synchronization: A Universal Concept in Nonlinear Sciences*, Vol. 12 (Cambridge University Press, Cambridge, 2003).
[17] J. M. Cruz, M. Rivera, and P. Parmananda, Phys. Rev. E **75**, 035201(R) (2007).
[18] D. K. Verma, H. Singh, A. Contractor, and P. Parmananda, J. Phys. Chem. A **118**, 4647 (2014).
[19] P. Kumar, D. K. Verma, P. Parmananda, and S. Boccaletti, Phys. Rev. E **91**, 062909 (2015).
[20] S. Nakata, K. Kayahara, M. Kuze, E. Ginder, M. Nagayama, and H. Nishimori, Soft Matter **14**, 3791 (2018).
[21] S. Sato, H. Sakuta, K. Sadakane, and K. Yoshikawa, ACS Omega **4**, 12766 (2019).
[22] M. Kapitaniak, K. Czolczynski, P. Perlikowski, A. Stefanski, and T. Kapitaniak, Phys. Rep. **541**, 1 (2014).
[23] A. B. Cawthorne, P. Barbara, S. V. Shitov, C. J. Lobb, K. Wiesenfeld, and A. Zangwill, Phys. Rev. B **60**, 7575 (1999).
[24] S. Strogatz, *Sync: The Emerging Science of Spontaneous Order* (Penguin UK, London, 2004).
[25] T. Banerjee and A. Basu, Phys. Rev. E **96**, 022201 (2017).
[26] D. Hansel and H. Sompolinsky, Phys. Rev. Lett. **68**, 718 (1992).
[27] F. Tu, X. Liao, and C. Li, in *International Symposium on Neural Networks* (Springer, Berlin, 2005), pp. 346–350.
[28] S. Boccaletti, V. Latora, Y. Moreno, M. Chavez, and D.-U. Hwang, Phys. Rep. **424**, 175 (2006).
[29] D. J. Watts and S. H. Strogatz, Nature **393**, 440 (1998).
[30] V. Pimienta and C. Antoine, Curr. Opin. Colloid Interface Sci. **19**, 290 (2014).
[31] G. Van der Mensbrugghe, Mém. Courronnés l'Acad. Roy. Sci. Belg. **34**, 1 (1869).
[32] S. Nakata, Y. Iguchi, S. Ose, M. Kuboyama, T. Ishii, and K. Yoshikawa, Langmuir **13**, 4454 (1997).
[33] C. Tomlinson, Proc. R. Soc. Lond. **11**, 575 (1860).
[34] M. Nagayama, S. Nakata, Y. Doi, and Y. Hayashima, Physica D **194**, 151 (2004).
[35] N. J. Suematsu, T. Sasaki, S. Nakata, and H. Kitahata, Langmuir **30**, 8101 (2014).
[36] N. J. Suematsu, Y. Ikura, M. Nagayama, H. Kitahata, N. Kawagishi, M. Murakami, and S. Nakata, J. Phys. Chem. C **114**, 9876 (2010).
[37] Y. Koyano, N. J. Suematsu, and H. Kitahata, Phys. Rev. E **99**, 022211 (2019).
[38] M. Frenkel, G. Whyman, E. Shulzinger, A. Starostin, and E. Bormashenko, Appl. Phys. Lett. **110**, 131604 (2017).
[39] Y. Koyano, M. Gryciuk, P. Skrobanska, M. Malecki, Y. Sumino, H. Kitahata, and J. Gorecki, Phys. Rev. E **96**, 012609 (2017).
[40] M. Frenkel, A. Vilk, I. Legchenkova, S. Shoval, and E. Bormashenko, ACS Omega **4**, 15265 (2019).
[41] J. Sharma, I. Tiwari, D. Das, P. Parmananda, V. S. Akella, and V. Pimienta, Phys. Rev. E **99**, 012204 (2019).
[42] M. I. Kohira, Y. Hayashima, M. Nagayama, and S. Nakata, Langmuir **17**, 7124 (2001).
[43] S. Nakata, Y. Doi, and H. Kitahata, J. Phys. Chem. B **109**, 1798 (2005).
[44] J. Rowlinson, Physica A **156**, 15 (1989).
[45] D. Blair and E. Dufresne, Particle-tracking code available at http://physics.georgetown.edu/matlab (2013).
[46] J. C. Crocker and D. G. Grier, J. Colloid Interface Sci. **179**, 298 (1996).
[47] See Supplemental Material at http://link.aps.org/supplemental/10.1103/PhysRevE.101.052202 for videos corresponding to 3 synchronized rotators on a line (1.mp4), 3 synchronized rotators on a triangle (2.mp4), 4 synchronized rotators on a line (3.mp4), 4 synchronized rotators on a square (4.mp4) and 5 synchronized rotators on a star geometry (5.mp4).
[48] R. Moessner and A. P. Ramirez, Phys. Today **59**, 24 (2006).
[49] Please refer to the document in the supplemental material [47] containing pictures of the actual experimental setup, the experimental and simulation phase plots corresponding to 4 synchronized rotators on a line and on a square and 5 synchronized rotators in a star geometry. Please note that the dynamics presented are for one of the representative configurations from each geometry.